Materials Advances

ROYAL SOCIETY OF CHEMISTRY

PAPER

View Article Online
View Journal | View Issue

Cite this: *Mater. Adv.*, 2025, 6, 5568

Bonding profiling of gapless ceramic V_2GaC/N MAX phases: a spectroscopic and dual theoretical approach†

Peter Ufondu, *[a] Sakshi, *[a] Teak D. Boyko, [b] Niels Kubitza, [c] Christina S. Birkel [cd] and Alexander Moewes [a]

The family of MAX phases is growing faster than ever, resulting in more than 340 reported members so far. Even though the variety of different M- and A-elements is overwhelming, the X-site of MAX phases is still mainly dictated by solely carbide-based materials, while nitrogen-based materials, such as nitrides and (carbo)nitrides account for below 10% in total. It follows that more profound studies comparing those three classical MAX phase groups are rare in the literature, particularly in terms of combining computational considerations with high-resolution spectroscopic experiments. Here, we report the electronic properties of three vanadium-based MAX phases: V_2GaC, V_2GaN, and the (carbo)nitride phase $V_2GaC_{1-x}N_x$. This investigation is carried out for C/N K-edge and the V L-edge using soft X-ray absorption (XAS) and emission spectroscopy (XES). We determine the x value to be 0.6 in the (carbo)-nitride $V_2GaC_{1-x}N_x$ phase. Additionally, we determine $V^{2.2+}$ as the formal oxidation state in all three phases using ligand field multiplet theory (LFMT) calculations. Our density functional theory (DFT) calculations indicate the presence of carbon vacancies in the V_2GaC phase. DFT and LFMT theoretical methods confirm that the V_2GaC has a higher degree of covalency than the V_2GaN phase. Also, Gallium interactions are the weakest with C/N and are entirely metallic.

Received 12th March 2025,
Accepted 27th June 2025

DOI: 10.1039/d5ma00222b

rsc.li/materials-advances

1. Introduction

MAX phases are an intriguing class of layered materials that combine characteristics of metals and ceramics. Conventionally, they are defined as hexagonal carbides and (carbo)nitrides with the general formula $M_{n+1}AX_n$ (n = 1, 2, 3, 4 (5, 6)), where M represents an early-to-mid transition metal (TM), A is an A-group element (primarily from groups 13, 14 and 15, such as IIIA, IVA and VA) or a late transition metal, and X is boron, carbon and/or nitrogen.[1–4] This classical definition has been softened over the recent years, since the possible "MAX-forming" elements have been drastically extended due to new inventive synthesis approaches, such as the element replacement approach.[5,6] Simultaneously, this led to an increase to more than 340 reported MAX phase members,[7] including all sorts of solid–solution variants, showing diverse exceptional properties such as superconductivity,[8,9] complex magnetic behavior,[10,11] or the role to serve as precursors for MXenes,[12,13] the 2D-siblings of MAX phases.

Despite the synthesis of so many new compounds within the last 10 years, the exploration of new nitrogen-containing MAX phases is still in its infancy, mainly dictated by the members already reported by Jeitschko *et al.*[14–16] in the late 1960s, particularly in terms of pure nitride materials. This is explained due to immense challenges during their synthesis, such as the high bonding energy of nitrogen or its gaseous physical state.[17] Studies on (carbo)nitrides are even more rare and mostly restricted to the Ti–Al–C–N system focusing on its synthesis, structural and stability behavior.[18–20] Here, only Yu *et al.* further took advantage of combining spectroscopy experiments and theory to investigate solid solution effects on the DOS to analyze the transport properties of the system.[18] However, over the last few years, new members of (carbo)nitride materials have been reported more frequently, for instance, by exploiting two-step hybrid solid-state approaches as shown for $Cr_2GaC_{1-x}N_x$,[21] $V_2GeC_{1-x}N_x$,[22] or the here described $V_2GaC_{1-x}N_x$,[23] system. Particularly, in the latter it was shown that a sol–gel based

[a] Department of Physics and Engineering Physics, University of Saskatchewan, 116 Science Place, Saskatoon S7N 5E2, Saskatchewan, Canada. E-mail: peter.ufondu@usask.ca, sakshi.s@usask.ca
[b] Canadian Light Source, 44 Innovation Blvd, Saskatoon, S7N 2V3, Saskatchewan, Canada
[c] Department of Chemistry and Biochemistry, Technische Universität Darmstadt, Peter-Grünberg-Straße 128, 64287 Darmstadt, Germany
[d] School of Molecular Sciences, Arizona State University, 727 E Tyler St. Tempe, AZ 85281, USA

† Electronic supplementary information (ESI) available. See DOI: https://doi.org/10.1039/d5ma00222b

synthesis approach combined with conventional solid-state techniques represents a valuable option to synthesize new (carbo)nitride MAX phase materials. Besides, even double-site solid–solution (carbo)nitrides have been reported, approaching complex/high-entropy solid–solution phases.[24] Nonetheless, both the nitrides and (carbo)nitrides are still outnumbered by about a factor of 10 compared to their carbide analogs, and the (carbo)nitride studies are mainly focused on their synthesis and application-based properties.[7] As shown with the latter examples and the comprehensive review article of Magnuson *et al.*,[25] the discussion of electronic properties going from carbide (carbo)nitride and towards nitride is rare, particularly high-resolution spectroscopy experiments combined with theory. This, however, could further help to get a better understanding of the influence of C/N mixing on the X-site and to provide more information towards tunable MAX phase properties solely based on X-site substitution.

In this work, the electronic properties and structural bonding of the 211 V–Ga–C–N system, including V_2GaC, V_2GaN, and $V_2GaC_{1-x}N_x$, are described.

Soft X-ray absorption spectroscopy (XAS) is used to study the electronic transition from core to partial unoccupied states, and X-ray emission spectroscopy (XES) probes the occupied electronic states. To complement our findings, resonant X-ray emission spectroscopy (rXES), which probes fundamental excitations,[26,27] is applied to the vanadium $L_{2,3}$-edges. These measurements are subsequently interpreted with our theoretical DFT for the K-edges of C and N and ligand field multiplet theory (LFMT) for the V L-edges. We determine the ratio of carbon and nitrogen in the $V_2GaC_{1-x}N_x$ phase. TM and groups VI and VII elements require different theories to study their electronic properties, which is why both theories are never (rarely) combined in the same publication.

We explain the bonding mechanisms in the V_2GaC and V_2GaN phases for Ga, V, C, and N. We also determine the formal oxidation state of the vanadium ion within the three phases.

2. Techniques

2.1. Experiment

The vanadium MAX samples were synthesized using the sol–gel method, details of which are described elsewhere.[23] The samples were affixed to the sample holder by pressing them into indium foil (freshly scraped to remove surface oxide). All XAS and XES spectra are collected at the resonant elastic and inelastic X-ray scattering (REIXS) beamline at the Canadian light source (CLS). Each scan for the XAS is collected simultaneously in total electron yield (TEY) and partial fluorescence yield (PFY) mode using both an SR570 current amplifier and a silicon drift detector (SDD) and are normalized to the incoming flux using the drain current from a gold mesh upstream of the sample. However, the TEY and PFY spectra of the measured samples look similar and, therefore, indicate that surface DOS and bulk DOS are similar. The V 2p XAS shown here is in TEY, while the C and N 1s XAS are displayed in the PFY. The energy resolution (ΔE) of the XAS measurements is 0.125 eV, 0.08 eV, and 0.04 eV for the oxygen (K-edge) and vanadium (L-edge), nitrogen (K-edge), and carbon (K-edge), respectively. XES spectra are collected using a Rowland-type grating spectrometer with an effective resolution of 450 meV. The XES spectra are calibrated using elastic peaks on the stainless steel sample holder. All measurements are performed in an ultra-high vacuum (1.0×10^{-9} Torr) with the relative angle between the spectrometer and the incoming beam at 90°. The incoming beam is 62.5° with respect to the sample surface.

2.2. Theory

The C and N K-edge electronic properties of the V_2GaC, V_2GaN, and $V_2GaC_{1-x}N_x$ are calculated using the WIEN2k (23.2) code,[28] a commercially available software package. All the DFT framework calculations implemented in the WIEN2k code are based on the augmented plane wave plus local orbital (APW + LO) method,[29] which considers all electrons (core and valence) with full potential to solve the Kohn–Sham equations.[30] For all the calculations, the generalized gradient approximation by Perdew, Burke, and Ernzerhof (PBE-GGA)[30] is used as an exchange–correlation function with an energy cutoff of −6 Ry to separate the core and valence electrons. A k-mesh of 750 ($15\times 15 \times 3$) is selected to stabilize total energy convergence per unit cell to 10^{-5} Ry and charge convergence of 10^{-3} e. Muffin tin radii (V: 2.11, Ga: 2.50, C/N 1.72) are almost touching each other in the interstitial region, with $R_{MT}K_{max}$ equal to 7. The theoretical XAS and XES spectra are calculated by multiplying the density of states with the transition matrix. To compare with the experimental spectrum, the calculated spectra are broadened by lifetime and instrumental broadening. In order to simulate the effect of core-hole screening we made $4 \times 4 \times 1$ supercell models (48 atoms) of all the materials and reduced the k-mesh proportionally (see Fig. S1, ESI†). Vacancy (impurity) calculations are also examined by removing (substituting) one or more atoms in the structure.

Due to the strong interaction of the 3d electrons, any DFT approximation is limited in properly describing the transition metal (TM) d electrons.[31] For that reason, the analysis of the V $L_{2,3}$-edges experimental spectra is carried out using the LFMT code that properly describes multiplets and takes into account resonant excitation mechanisms such as energy loss and charge transfer. It is indispensable in interpreting spectral features by fitting calculated to experimental spectra and extracting parameters such as crystal field strength (10 Dq), spin–orbit coupling (ζ_{2p}, ζ_{3d}), Slater integral (F_{dd}, F_{pd} and G_{pd}), on-site Coulomb interaction (U), charge transfer energy (Δ) and the hopping strength of the 3d orbital (V_e and $V_{t_{2g}}$) in an O_h symmetry. Our LFMT calculations are performed using the Quanty Code,[32–35] a software package for simulating d and f electron systems.

The model Hamiltonian in O_h symmetry used for the calculations is described elsewhere.[26] During the simultaneous XAS and RIXS calculations, a Powell fitting algorithm[36] is used to optimize the fitted parameters, and a Gaussian profile of 0.8 eV (FWHM) is used to broaden the calculated spectra to

account for the experimental resolution (see ESI,† for the GitHub link to the LFMT code and Table S2, ESI†).

3. Results and discussion

3.1. Vanadium L-edge

In Fig. 1, key peaks common to all the samples are labeled a through f, corresponding to either hybridization between the TM and ligand or specific electronic transition states.

Fig. 1(B) shows a peak, labeled d, at approximately 513.9 eV, with the highest count in the V_2GaC, compared to $V_2GaC_{1-x}N_x$, and the lowest in V_2GaN. We attribute this peak to the lower-lying, triply degenerate t_{2g} set of V 3d orbitals.[37,38] The trend in peak d counts indicates a weaker covalent bond in V_2GaN than in V_2GaC which corresponds to the hybridization strength in the t_{2g} orbitals. This is consistent with our electron density calculations discussed later. The increased count and broader area of peak d in $V_2GaC_{1-x}N_x$ suggest the presence of bonding contributions from both C and N ligands in this sample (multi-center bonding). Another notable peak, labeled e, appears across all three samples at the same energy but is separated from d by approximately 2 eV. This peak arises from the higher-energy double-degenerate e_g set of V 3d orbitals directed toward the ligand C, N, and (C, N) point charges. Feature f, representing the V L_2-edge ($P_{1/2}$), is well reproduced in the calculated spectra despite the presence of a strong Coster–Kronig transition.

To quantify the relative concentrations of carbon and nitrogen in $V_2GaC_{1-x}N_x$, we acknowledge that vanadium retains identical metal-carbon/nitrogen coordination (M_6X) within both V_2GaC and V_2GaN phases. Thus, a rigorous comparison can be achieved by constructing a linear combination of the experimentally observed and theoretically calculated spectra for V L-edge in V_2GaC and V_2GaN. By systematically varying the weights of each component in the linear combination, we can directly compare these composite spectra to the measured spectra of $V_2GaC_{1-x}N_x$.

The optimal spectral match is achieved with a composition of 40% carbon and 60% nitrogen in $V_2GaC_{1-x}N_x$. A strong correspondence is observed between the calculated V L-edge spectrum for $V_2GaC_{1-x}N_x$ (solid black line) and a composite spectrum derived from a linear combination of 40% V_2GaC and 60% V_2GaN (solid green line), where each phase consists of 80% V^{2+} and 20% V^{3+}. Furthermore, both calculated spectra closely agree with the experimentally measured spectrum (solid red line). The presence of the 20% V^{3+} state might be due to surface oxidation and can be seen in the higher energy region of the non-resonant X-ray emission spectrum of Fig. S2 (ESI†). This highlights the accuracy of such linear combinations in reproducing experimental spectra and reinforces the validity of our experimental measurements and LFMT models. Given the high level of agreement between the experimental and calculated V L-edge spectra, we assign an oxidation state of 2.2+ for vanadium in all samples. Supporting data, including the calculated XAS for V^{2+} and V^{3+} ions across all samples, along with the various experimental spectra ratios, are provided in the ESI† (Fig. S2, S4 and S5). To further validate this oxidation state and to characterize additional spectral features, we performed energy-resolved excitations at the L_3-edge, exciting at the t_{2g} and e_g peak regions selectively.

Fig. 1(A) presents the measured rXES spectra, excited using photon energies specified as marked in the XAS spectra and labeled as d (513.79 eV for V_2GaC and $V_2GaC_{1-x}N_x$, and 514.20 eV for V_2GaN) and e (516.01 eV for V_2GaC and V_2GaN, and 516.20 eV for $V_2GaC_{1-x}N_x$). The rXES spectra are primarily characterized by strong V fluorescence counts labeled as a and b. As the excitation energy increases, these features shift to lower energies, leading to a decrease in the count of the elastic scattering feature labeled c at 0 eV.

Features a and b exhibit a shift corresponding to the transition from the lower t_{2g} excitation energy to the higher e_g excitation energy, highlighting the energy difference between these states. We attribute peak a to fluorescence arising from the V–N p orbital transitions, while peak b corresponds to transitions between the V 2p and Ga p states.

In Table S1 (ESI†), the values of U_{pd-dd} for V^{2+} and V^{3+} states in the samples are used to quantify the degree of covalency. The U_{pd-dd} parameter directly impacts the degree of electron localization in the vanadium d orbitals. A stronger U_{pd-dd} value, such as the 2.00 eV observed for both $V_2GaC_{1-x}N_x$ and V_2GaN, tends to localize electrons in the d orbitals orbitals. This localization results from the greater repulsive force, limiting their overlap with ligand orbitals and reducing their participation in bonding.

In contrast, the lower U_{pd-dd} value of 1.83 eV observed for V_2GaC suggests a weaker Coulomb interaction. As a result, more electrons participate in bonding, enhancing covalency and facilitating more significant overlap and hybridization with the neighboring ligand orbitals. This increased electron

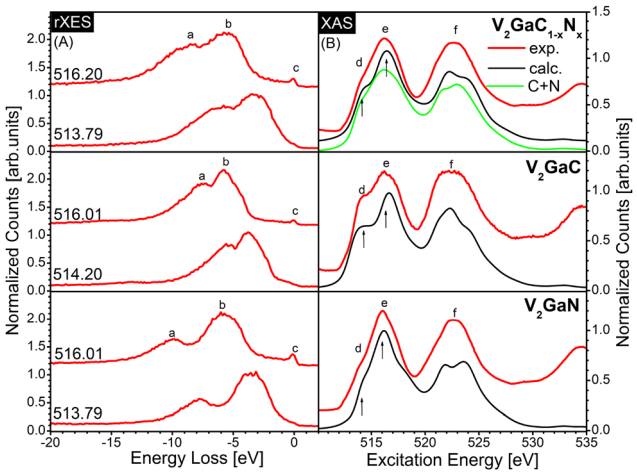

Fig. 1 Vanadium $L_{2,3}$-edge experimental spectrum (red) compared with the calculated spectrum (black). (A) Resonant X-ray emission spectroscopy (rXES) in the energy loss and (B) X-ray absorption spectroscopy (XAS) spectra plotted for V_2GaN, V_2GaC, and $V_2GaC_{1-x}N_x$. The calculated spectra are shown as solid black lines, while the solid green line represents a linear combination of 60% V_2GaN and 40% V_2GaC. Each phase (V_2GaN and V_2GaC) consists of 80% V^{2+} and 20% V^{3+}, capturing the mixed valence nature of vanadium. The 0 eV energy indicates the excitation energy.

delocalization contributes to the stronger covalent character observed in V_2GaC.

3.2. Carbon and nitrogen K-edges

The combined presence of carbon and nitrogen in the $V_2GaC_{1-x}N_x$ allows to extract the separate effects for both carbon and nitrogen. In Fig. 2, we discuss the calculated and experimental spectra for the C and N K-edges. The comparison spectra show an excellent agreement between the calculations and measurements. We will first focus on the C K-edge.

Fig. 2(B) and (D) show the measured XAS spectra (red) for the samples containing carbon in $V_2GaC_{1-x}N_x$ and V_2GaC, respectively. The C Kα 1s XAS spectra of both samples are identical due to the nearly identical bonding environment. The XAS of $V_2GaC_{1-x}N_x$ and V_2GaC consists of two sharp distinct features, labeled as c and d followed by less intense broad features e and f. The key difference between the two is the detection of shoulder features d′ in $V_2GaC_{1-x}N_x$ and e′ in V_2GaC, respectively. These pre- and post-features are due to the modification of carbon bonding in the samples. Peak c and d are attributed to the transition of C 1s to C 2p–V 3d hybridization states with a 0.5 eV shift to the left.[39,40] However, C vacancies are likely to contribute to feature c, which will be discussed later. We assign peak d to π* anti-bonding, which had been reported to be between 284 eV to 288 eV.[41] The peaks *e* in $V_2GaC_{1-x}N_x$ and V_2GaC are due to carbon σ*,[41] anti-bonding. The energy difference of 1.5 eV between the two samples is observed due to the presence of nitrogen bonding in $V_2GaC_{1-x}N_x$ and as a result, shows a sharper e_g peak in the V L-edge of $V_2GaC_{1-x}N_x$ than its parent carbide phase. The broadened feature f at 296 eV is due to the 1s to unoccupied orbitals that also involve contributions from C (2p, 3p) and V (3d, 4s) states.

The simulated spectra (black) for V_2GaC and $V_2GaC_{1-x}N_x$ are compared along with the measurement (red). The impact of the core-hole (solid) is clearly illustrated when compared with the ground state (dashed) in the calculation. The simulated C 1s core-hole spectrum of V_2GaC (see Fig. 2(D)) shows good agreement with the measured spectra. The general spectral shape and mainly all the features are well reproduced except c. The feature c is not present in the calculated (black) XAS spectrum, which is simulated with the experimentally determined crystalline structure. This small disagreement between calculated and measured spectra leads to further investigation into the structure. The work of Etzkorn *et al.*[42] has shown a C-defect in the V–Al carbide phases. Peak c is reproduced in the vacancy calculation (blue), where we removed one carbon atom in the supercell to create a vacancy. However, it is slightly shifted to higher energy by 0.81 eV. Moreover, the impurity calculation is also performed by substitution of one carbon atom with an oxygen atom at the same position where we created the vacancy. The resulting calculated spectrum is unsuccessful at reproducing c feature (see ESI,† Fig. S6). This indicates that c is caused by a carbon vacancy and not affected by the presence of oxygen in V_2GaC.

Fig. 2(A) and (C) show the C Kα non-resonant XES (nXES) excited above the C K-edge binding energy at (320 eV). The C Kα nXES spectra of both $V_2GaC_{1-x}N_x$ and V_2GaC show similar shape with an energy shift of 1 eV. The XES spectra consist of strong feature a, which is due to a large amount of C 2p states present at the valence band (VB).

The presence of shoulder a′ in the case of V_2GaC is the significant contrast between the two samples. This is due to the C 2p states, which show some degree of hybridization with the neighboring atoms (Ga and V). The low intense peak b and shoulder b′ are assigned to a few states present at the Fermi level. The calculated spectra of both samples match the measured emission spectra.

We now turn our analysis to the N K-edge spectra. Fig. 2ii shows the N 1s XAS and Kα XES of $V_2GaC_{1-x}N_x$ and V_2GaN.

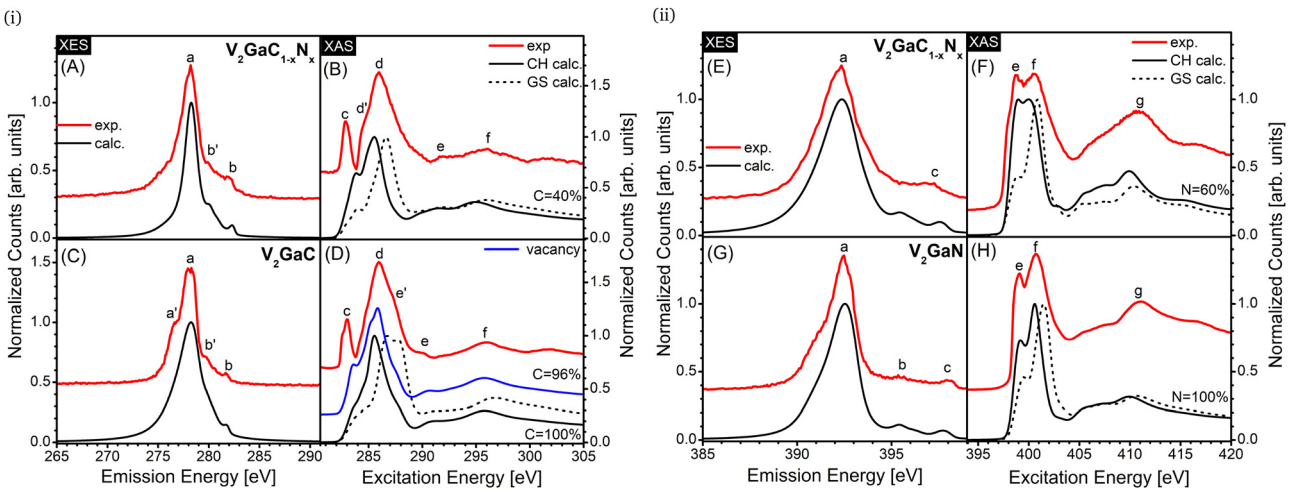

Fig. 2 Experimental (red) and calculated (black) spectra for the K-edges. (i) Shows the C K-edge while (ii) presents the N K-edge. Panel (A), (B), (E) and (F) are $V_2GaC_{1-x}N_x$ XES and XAS at the C and N K-edges, respectively. Experimental spectra are compared with the calculated spectra of 40% (60%) carbon (nitrogen) in $V_2GaC_{1-x}N_x$. (C) and (D) represent the measured and calculated XES and XAS spectra of carbon in V_2GaC without vacancy (black) and with vacancy 4% (blue), whereas (G) and (H) illustrate N K-edge XES and XAS spectra of V_2GaN alongside the calculated spectra. In the XAS, the dashed line denotes ground state calculations, while the solid indicates the core-hole.

The DFT calculated spectra (black) are in excellent agreement with the measured spectra (red) for both samples. The peaks e and f are from the transition of 1s electrons to the hybridized N p–V d. The lower energy feature e is assigned t_{2g} while the higher energy peak is e_g.[39,43] Both samples exhibit the same spectral features (e, f, g) at the same energy but one observes that the ratio of the e to f feature is different. This variation in the ratio is due to the t_{2g} electron density evenly redistributed in $V_2GaC_{1-x}N_x$. The broad feature g is an account of the contribution from 2p and 3p orbitals of nitrogen and 3d and 4s states of vanadium. The DFT simulated spectra reproduce every feature with high accuracy of the spectral height in XAS for both samples.

Similarly, the calculated and measured N Kα nXES spectra of $V_2GaC_{1-x}N_x$ and V_2GaN agree well. It is noted that the measured nXES spectra of $V_2GaC_{1-x}N_x$ and V_2GaN have one sharp peak at 392 eV showing the 2p bonding state of nitrogen. The features b and c near the Fermi level are due to the hybridization of 2p with the vanadium d and gallium s, p, d states in the upper VB. One can see that the feature b is not prominent in $V_2GaC_{1-x}N_x$ as compared to V_2GaN due to the variation in the electron density of nitrogen. Also, the relative energy of feature c is shifted more towards the Fermi energy in the case of V_2GaN. This shift is due to the nitrogen bonding environment being different in both samples.

The calculated XAS and XES spectra for the $V_2GaC_{1-x}N_x$ produced all the expected spectral features with the correct relative intensities. Our DFT calculations indicate that the structure contains 40% carbon and 60% nitrogen, resulting in the configuration $V_2GaC_{0.4}N_{0.6}$. This is further supported by our V $L_{2,3}$-edge measurements and agreed well with the synthesis article by Kubitza *et al.*[23]

The DOS provides a more detailed analysis of the electronic structure of the samples and where the valence electrons reside. The pDOS of each element is interesting and illustrated in Fig. 3i. There are clearly two distinct bands available in the valence band (VB). The lower energy in the valence band is due to the s character in the carbon and nitrogen while the p orbital contributes to the higher energy features. This can be associated with the σ bond. Ga $3d^{10}$ states at −15 eV are highly localized, suggesting no bonding. The hybridization of V d and p states in C and N between −7 to −3 eV shows the degree of covalency in both cases. Ga p states hybridize[44] weakly with V d states at −2.5 eV, which is also replicated in our electron density map Fig. 3iii. The Fermi level (0 eV) is dominated by the V d states with the contribution of the Ga p, d orbitals indicating that there is no bandgap and suggesting metallicity in the compounds. In the conduction band, the total DOS is dominated by V d states in each sample. The Ga p, d characters are fairly distributed throughout, while for the C and N atoms, the p orbital contributes significantly more than s states.

Fig. 3ii shows the calculated total DOS for all nonequivalent atoms present in (carbo)nitride $V_2GaC_{0.4}N_{0.6}$ unit cell. The structure is designed and optimized to represent the synthesized sample. The unit cell has ten vanadium, five gallium, and four nitrogen and carbon inequivalent sites, respectively.

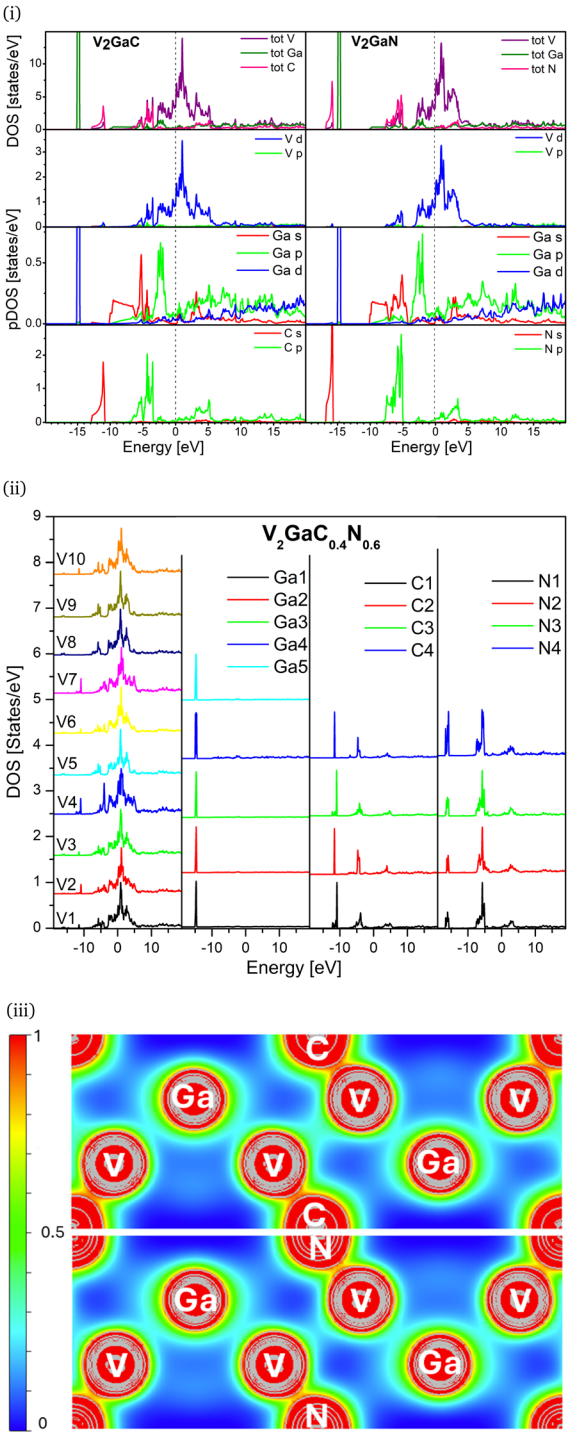

Fig. 3 (i) Calculated density of states for V_2GaC (on the left) and V_2GaN (on the right). The top panel shows the total density of states, followed by the partial DOS of V, Ga, and C/N, which are color-coded. (ii) Represents calculated total DOS for nonequivalent atom sites present in (carbo)nitride phase $V_2GaC_{0.4}N_{0.6}$. (iii) Calculated valence electron density of V_2GaC (top) and V_2GaN (bottom) in the (110) plane. This plane was selected to visualize the V, Ga, and C/N bonding scheme. The map is depicted by an isosurface of 0.827 with a minimum and maximum cutoff value of 0.018 and 0.998, respectively.

We find good agreement between our measurements and calculations. It is important to highlight that the calculated

$V_2GaC_{0.4}N_{0.6}$ structure replicates the combined DOS features of both V_2GaC and V_2GaN. The sites V2, V4 and V7 have the same peaks at −10.93 eV as V_2GaC. Meanwhile sites V5, V8 and V9 have the same energy peak −16.15 eV as V_2GaN. Additionally, sites V1, V3, V6 and V10 have energy features that are consistent with those observed in both V_2GaN and V_2GaC. The DOS for Ga, C, and N at all inequivalent sites is identical to that of the parent samples. This indicates that the electronic environment for Ga remains unaffected by the combined neighboring atoms, suggesting that the novel (carbo)nitride retains the electronic properties of both parent materials.

Now, the electron density color map in Fig. 3iii provides in-depth pictorial information to verify the novel bonding for Ga, V, C, and N in the systems. The maxima of the electron density of the Ga atoms are symmetric around the center, indicating that the electron density is confined to the atom. This confirms that the Ga interactions are the weakest with C/N and entirely metallic in both V_2GaC and V_2GaN structures. The almost spherical contours of the vanadium and carbon/nitrogen show a slight bending of contours towards each other in the system. The cyan color indicates the change in electron density between V and C/N atoms, suggesting that electron density is shared (light red) within the sample. This observation aligns with the expected covalent characteristics of the samples. However, conclusions driven by the color in the map for both samples reveal that the V–C bond exhibits a greater degree of covalency than the V–N bond, supporting the results obtained from our LFMT calculation. This is further supported by electron localization function[45] (ELF) in Fig. 4 and Bader charge analysis[46] in Table. S3 (ESI†).

In Fig. 4, the ELF is visualized using a color contour plot ranging from blue to red (0 to 1). The delocalized electrons are projected in the lesser than 0.5. The regions shaded yellow-red correspond to high ELF values approaching 1.0, indicating strong electron localization, most notably around the Ga atoms. These observations are consistent with the Bader charge analysis presented in Table S3 (ESI†), which reveals significant charge transfer from vanadium to the carbon and nitrogen atoms, with net charges of +1.52 *e* and +1.48 *e*, respectively.

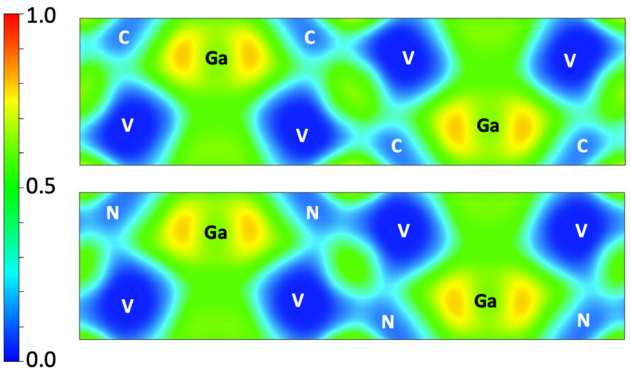

Fig. 4 Electron localization function (ELF) maps for V_2GaC (top) and V_2GaN (bottom) MAX phases, illustrating the electron distribution and bonding nature in these layered ternary compounds.

This charge redistribution aligns with the high electronegativities of C and N. Notably, the ELF indicates a greater electron accumulation near the V–C bond compared to the V–N bond, suggesting stronger and more directional bonding in the former.

4. Conclusion

In this work, we explore the bonding and electronic properties of three vanadium-based MAX phases: V_2GaC, V_2GaN, and the (carbo)nitride phase $V_2GaC_{1-x}N_x$. The parent models V_2GaC and V_2GaN exhibit distinct electronic features. V_2GaC reveals a carbon vacancy in the structure, while V_2GaN demonstrates significant splitting into t_{2g} and e_g bonding states. All the analysis indicates that there is no band gap in the samples, which reveals their metallic character. In the (carbo)nitride phase $V_2GaC_{1-x}N_x$, we determine that the concentration of carbon and nitrogen are 40% and 60%, respectively with a chemical formula $V_2GaC_{0.4}N_{0.6}$. These numbers validate the work by Kubitza *et al.*[23] Also, we show that $V_2GaC_{0.4}N_{0.6}$ retain the combined electronic properties as the parent samples. We examine the bonding mechanism in both V_2GaC and V_2GaN phases, emphasizing that the V_2GaC has a higher degree of covalency than V_2GaN. This is in contrast to typical electronegativity differences between carbon and nitrogen atoms.[47] Among all atoms in the samples, V–Ga shows the weakest interaction with strong electron localization (metallic bonding) in both V_2GaC and V_2GaN. Furthermore, we established a formal oxidation state of $V^{2.2+}$ for vanadium across all three MAX phases.

Author contributions

Peter Ufondu: investigation, methodology, visualization, software, writing – original draft. Sakshi: investigation, methodology, visualization, writing – original draft. Teak D. Boyko: investigation, resources. Niels Kubitza: investigation, validation. Christina S. Birkel: project administration, validation. Alexander Moewes: project administration, supervision, validation and correction, funding acquisition.

Conflicts of interest

There are no conflicts to declare.

Data availability

The authors confirm that the data supporting the findings of this study are available within the article and its ESI.†

Acknowledgements

This work is supported by the Natural Sciences and Engineering Research Council of Canada (NSERC), the Canada Research Chairs (CRC) program, the interdisciplinary Network for the

Synchrotron: Promoting Innovation, Research, and Enrichment (NSERC CREATE) program, and the Deutsche Forschungsgemeinschaft (DFG, German Research Foundation) within CRC/TRR 270, project B03. All of the experimental research described in this paper was performed at the REIXS beamline of the Canadian Light Source, a national research facility of the University of Saskatchewan (USask), which is supported by the Canada Foundation for Innovation (CFI), the Natural Sciences and Engineering Research Council (NSERC), the Canadian Institutes of Health Research (CIHR), the Government of Saskatchewan, and the University of Saskatchewan. This research was enabled by computational support provided by the Digital Research Alliance of Canada (alliancecan.ca), and Plato (USask), which is managed by ICTs Advanced Research Computing (ARC) team.

References

1 M. W. Barsoum, *Prog. Solid State Chem.*, 2000, **28**, 201–281.
2 N. Kubitza, C. Büchner, J. Sinclair, R. M. Snyder and C. S. Birkel, *ChemPlusChem*, 2023, **88**, e202300214.
3 M. A. Hadi, *J. Phys. Chem. Solids*, 2020, **138**, 109275.
4 M. A. Hadi, *J. Phys. Chem. C*, 2023, **127**, 23489–23503.
5 M. Li, J. Lu, K. Luo, Y. Li, K. Chang, K. Chen, J. Zhou, J. Rosen, L. Hultman, P. Eklund, P. O. Persson, S. Du, Z. Chai, Z. Huang and Q. Huang, *J. Am. Chem. Soc.*, 2019, **141**, 4730–4737.
6 H. Ding, Y. Li, M. Li, K. Chen, K. Liang, G. Chen, J. Lu, J. Palisaitis, P. O. Persson, P. Eklund, L. Hultman, S. Du, Z. Chai, Y. Gogotsi and Q. Huang, *Science*, 2023, **379**, 1130–1135.
7 M. Dahlqvist, M. W. Barsoum and J. Rosen, *Mater. Today*, 2024, **72**, 1–24.
8 A. Bortolozo, O. SantAnna, C. dos Santos and A. Machado, *Solid State Commun.*, 2007, **144**, 419–421.
9 A. Bortolozo, G. Serrano, A. Serquis, D. Rodrigues, C. dos Santos, Z. Fisk and A. Machado, *Solid State Commun.*, 2010, **150**, 1364–1366.
10 J. P. Siebert, S. Mallett, M. Juelsholt, H. Pazniak, U. Wiedwald, K. Page and C. S. Birkel, *Mater. Chem. Front.*, 2021, **5**, 6082–6091.
11 C. M. Hamm, J. D. Bocarsly, G. Seward, U. I. Kramm and C. S. Birkel, *J. Mater. Chem. C*, 2017, **5**, 5700–5708.
12 M. Naguib, O. Mashtalir, J. Carle, V. Presser, J. Lu, L. Hultman, Y. Gogotsi and M. Barsoum, *ACS Nano*, 2012, **6**, 1322–1331.
13 M. Naguib, M. W. Barsoum and Y. Gogotsi, *Adv. Mater.*, 2021, **33**, 2103393.
14 W. Jeitschko, H. Nowotny and F. Benesovsky, *Monatsh. Chem.*, 1964, **95**, 178–179.
15 W. Jeitschko, H. Nowotny and F. Benesovsky, *Monatsh. Chem.*, 1964, **95**, 156–157.
16 O. Beckmann, H. Boller, H. Nowotny and F. Benesovsky, *Monatsh. Chem.*, 1969, **100**, 1465–1470.
17 A. Greenaway, C. Melamed, M. Tellekamp, R. Woods-Robinson, E. Toberer, J. Neilson and A. Tamboli, *Annu. Rev. Mater. Res.*, 2021, **51**, 591–618.
18 W. Yu, V. Mauchamp, T. Cabioch, D. Magne, L. Gence, L. Piraux, V. Gauthier-Brunet and S. Dubois, *Acta Mater.*, 2014, **80**, 421–434.
19 T. Cabioch, P. Eklund, V. Mauchamp and M. Jaouen, *J. Am. Ceram. Soc.*, 2012, **32**, 1803–1811.
20 M. A. Pietzka and J. C. Schuster, *J. Am. Ceram. Soc.*, 1996, **79**, 2321–2330.
21 N. Kubitza, I. Huck, H. Pazniak, C. Kalha, D. Koch, B. Zhao, P. K. Thakur, T.-L. Lee, A. A. Riaz, W. Donner, H. Zhang, B. Moss, U. Wiedwald, A. Regoutz and C. S. Birkel, *J. Mater. Chem. C*, 2024, **12**, 7552–7561.
22 N. Kubitza, B. Beckmann, S. Jankovic, K. Skokov, A. A. Riaz, C. Schlueter, A. Regoutz, O. Gutfleisch and C. S. Birkel, *Chem. Mater.*, 2024, **36**, 1375–1384.
23 N. Kubitza, A. Reitz, A.-M. Zieschang, H. Pazniak, B. Albert, C. Kalha, C. Schlueter, A. Regoutz, U. Wiedwald and C. S. Birkel, *Inorg. Chem.*, 2022, **61**, 10634–10641.
24 Z. Du, C. Wu, Y. Chen, Q. Zhu, Y. Cui, H. Wang, Y. Zhang, X. Chen, J. Shang, B. Li, W. Chen, C. Liu and S. Yang, *Adv. Energy Mater.*, 2022, **12**, 2103228.
25 M. Magnuson and M. Mattesini, *Thin Solid Films*, 2017, **621**, 108–130.
26 P. Ufondu, T. D. Boyko, M. M. Pointner, L. Eisenburger, W. Schnick and A. Moewes, *J. Mater. Chem. C*, 2024, **12**, 4392–4398.
27 P. Ufondu, Sakshi, T. D. Boyko, M. M. Pointner, W. Schnick and A. Moewes, *Adv. Sci.*, 2025, **12**, 2412830.
28 K. Schwarz, P. Blaha and G. Madsen, *Comput. Phys. Commun.*, 2002, **147**, 71–76.
29 P. Blaha, K. Schwarz, G. Madsen, D. Kvasnicka, J. Luitz, R. Laskowski, F. Tran and L. Marks, *Tech. Univer. Wien*, 2018, 3–9501031.
30 J. P. Perdew, K. Burke and M. Ernzerhof, *Phys. Rev. Lett.*, 1996, **77**, 3865–3868.
31 P. Blaha, K. Schwarz, F. Tran, R. Laskowski, G. Madsen and L. Marks, *J. Chem. Phys.*, 2020, **152**, 0021–9606.
32 M. W. Haverkort, M. Zwierzycki and O. K. Andersen, *Phys. Rev. B: Condens. Matter Mater. Phys.*, 2012, **85**, 165113.
33 Y. Lu, M. Höppner, O. Gunnarsson and M. W. Haverkort, *Phys. Rev. B: Condens. Matter Mater. Phys.*, 2014, **90**, 085102.
34 M. W. Haverkort, G. Sangiovanni, P. Hansmann, A. Toschi, Y. Lu and S. Macke, *EPL*, 2014, **108**, 57004.
35 M. W. Haverkort, *J. Phys.:Conf. Ser.*, 2016, **712**, 012001.
36 M. J. D. Powell, *Comput. J.*, 1964, **7**, 155–162.
37 T. M. Tolhurst, B. Leedahl, J. L. Andrews, P. M. Marley, S. Banerjee and A. Moewes, *Phys. Chem. Chem. Phys.*, 2016, **18**, 15798–15806.
38 D. Maganas, M. Roemelt, T. Weyhermüller, R. Blume, M. Hävecker, A. Knop-Gericke, S. DeBeer, R. Schlögl and F. Neese, *Phys. Chem. Chem. Phys.*, 2014, **16**, 264–276.
39 R. Kapoor, S. T. Oyama, B. Friihberger, B. D. DeVries and J. G. Chen, *Catal. Lett.*, 1995, **34**, 179–189.
40 G. Abrasonis, M. Berndt, M. Krause, K. Kuepper, F. Munnik, A. Kolitsch and W. Möller, *J. Phys. Chem. C*, 2008, **112**, 17161–17170.
41 J. Stöhr, *NEXAFS Spectroscopy*, Springer, 1992.

42 J. Etzkorn, M. Ade and H. Hillebrecht, *Inorg. Chem.*, 2007, **46**, 7646–7653.
43 M. Krbal, A. Kolobov, P. Fons, K. Mitrofanov, Y. Tamenori, B. Hyot, B. Andre and J. Tominaga, *J. Alloys Compd.*, 2017, **704**, 254–259.
44 A. Bouhemadou, *Solid State Sci.*, 2009, **11**, 1875–1881.
45 P. Giannozzi, S. Baroni, N. Bonini, M. Calandra, R. Car, C. Cavazzon, D. Ceresoli, G. L. Chiarotti, M. Cococcioni, I. Dabo and A. Dal Corso, *et al.*, *J. Phys. Condens. Matter*, 2009, **21**, 395–502.
46 W. Tang, E. Sanville and G. Henkelman, *J. Phys. Condens. Matter*, 2009, **21**, 084–204.
47 M. Magnuson, *MRS Proc.*, 2007, **1023**, 901.